Exploring generic principles of compartmentalization in a developmental in-vitro model

Pierre-Yves Gires[*,‡], Mithun Thampi[‡], Sebastian W. Krauss[‡], Matthias Weiss[§]

Experimental Physics I, University of Bayreuth, Universitätsstr. 30, D-95447 Bayreuth, Germany

[*]Present address: Depixus SAS, 3/5 Impasse Reille, 75014 Paris, France
[‡]These authors contributed equally.
[§]Author for correspondence: Matthias Weiss (matthias.weiss@uni-bayreuth.de)

Abstract

Self-organization of cells into higher-order structures is key for multicellular organisms, e.g. via repetitive replication of template-like founder cells or syncytial energids. Yet, very similar spatial arrangements of cell-like compartments ('protocells') are also seen in a minimal model system of Xenopus egg extracts in the absence of template structures and chromatin, with dynamic microtubule assemblies driving the self-organization process. Quantifying geometrical features over time, we show here that protocell patterns are highly organized with a spatial arrangement and coarsening dynamics like two-dimensional foams but without the long-range ordering expected for hexagonal patterns. These features remain invariant when enforcing smaller protocells by adding taxol, i.e. patterns are dominated by a single, microtubule-derived length scale. Comparing our data to generic models, we conclude that protocell patterns emerge by simultaneous formation of randomly assembling protocells that grow at a uniform rate towards a frustrated arrangement before fusion of adjacent protocells eventually drives coarsening. The similarity of protocell patterns to arrays of energids and cells in developing organisms, but also to epithelial monolayers, suggests generic mechanical cues to drive self-organized space compartmentalization.

Keywords: Xenopus egg extract, pattern formation, nonequilibrium, self-organization, foam, hyperuniformity

SUMMARY STATEMENT

Cell-like arrays in self-organizing egg extracts feature a dynamically coarse-graining geometry like two-dimensional foams without long-range order. Similar results from embryos and tissues suggest common principles of space compartmentalization.

INTRODUCTION

A hallmark of living matter is the ability to form and replicate well-defined cellular entities that eventually constitute a multicellular organism. In fact, embryogenesis is supposedly one of the most complex self-organization phenomena in nature as systems form dynamically adapting structures across multiple length and time scales, far from thermal equilibrium: Individual molecules self-assemble in few milliseconds into higher-order complexes on the nanoscale, eventually leading to micron-sized organelles that structure individual cells on length scales of $\sim 10\ \mu$m within periods of minutes to hours. Each cell converts about 10^7 ATP molecules per second to dynamically maintain its ordered state while joining a collective arrangement with neighbors into extended tissues. Ultimately, living animals emerge that are eight to nine orders of magnitude larger than their molecular constituents, and they may exist for a life span of up to hundred years. It appears therefore appropriate to call embryogenesis a true multiscale and non-equilibrium problem that mankind is just about to explore in its whole complexity. In fact, arriving at an in-depth understanding for any one of these two facets, including the development of proper theory and tools, is already a major and still very open challenge in the quantitative natural sciences.

A fair number of developmental model organisms, from worms (e.g. *Caenorhabditis elegans*) and flies (e.g. *Drosophila melanogaster*) up to fish (e.g. *Danio rerio*) and mammals (e.g. *Mus musculus*), have been instrumental in revealing key steps of embryogenesis. These include, but are not restricted to, pivotal morphogen signaling pathways that direct development and spatial organization via self-organized biochemical gradients, hence bridging length and time scales from the molecular to the organismal level: Relying on the concept of Turing patterns and related mechanisms (Turing, 1952; Kondo and Miura, 2010), morphogen gradients may single out preferred directions and loci, e.g. during the establishment of body axes in *C. elegans* (Goehring et al., 2011; Gross et al., 2019) or mesoderm segmentation in mice (Lauschke et al., 2013; Sonnen et al., 2018).

Despite their tremendous success, developmental model organisms often come along with inherent limitations. Studying the dynamic evolution of an embryo, for instance, may require the use of light microscopy techniques, requiring specimen to be sufficiently transparent. While this is mostly given for *C. elegans* or *D. rerio*, imaging the development of *Drosophila* at early stages can be challenging due to the opaque yolk, requiring advanced imaging modalities (Krzic et al., 2012). In addition, confining envelopes like the chitin egg shell of *C. elegans*, often hamper a controlled perturbation of the embryonic development via the addition of chemicals and pharmaceuticals at specific stages. Moreover, mechanical boundary conditions within the embryo, e.g. an anisotropically varying tissue stiffness, may be key for certain processes (Koser et al., 2016; Franze, 2020), but are hard to access or to manipulate in the intact organism. Last but not least, any model organism is typically much more complex than the particular problem that is studied with it, and insights derived from one model may not be transferable to other organisms. Well-defined and accessible *in-vitro* assays for studying generic developmental processes, preferably minimal systems with greatly reduced complexity, are therefore an attractive approach to complement the work with model organisms.

A high degree of accessibility facilitates, for instance, the exploration of mechanobiology aspects since mechanical cues and boundary conditions become more susceptible to external control. In fact, the mutual action of mechanical and biochemical processes has gained considerable attention in recent years, not least in the context of embryogenesis: Cell positioning during the early development of *C. elegans* is, for example, strongly guided by mechanical cues between cells and the confining egg shell (Fickentscher et al., 2013; 2016; Yamamoto and Kimura, 2017), and a fluid-to-solid jamming transition has been shown to facilitate vertebrate body axis elongation (Mongera et al., 2018). Going beyond these examples, the fundamental ability of organisms to achieve a highly ordered spatial organization of cellular entities is a stunning and very general phenomenon that invokes mechanobiology: Fly wings and retinae, like many other (embryonic) tissues, generate near-hexagonal cell patterns (Classen et al., 2005; Sugimura and Ishihara, 2013; Hayashi and Carthew, 2004), the syncytium of *Drosophila* and oocytes of the marine ascidian *Phallusia mammillata* feature a regularly ordered, not necessarily enveloped compartmentalization (de Carvalho et al., 2022; Guignard et al., 2020; Khetan et al., 2021), and even monolayers of MDCK culture cells arrange in a near-periodic lattice on large length scales (Kaliman et al., 2021).

Inspired by these observations in different models, we strived for a minimal self-organizing system that is capable of showing a similar spatial organization on super-cellular length scales. Furthermore, we aimed at a system without a confining envelope to facilitate physical and chemical manipulations. Xenopus egg extracts that have frequently been used to explore fundamental cell-biological and developmental processes, e.g. the formation and interactions of microtubule asters and mitotic spindles (Good et al., 2013; Mitchison et al., 2012; 2015), nicely satisfy this criterion, and we therefore have employed a recently introduced *in-vitro* assay that is based on extracts from unfertilized *Xenopus laevis* eggs (Cheng and Ferrell, 2019). In contrast to embryonic development that is driven by replication and inheritance of a fertilized oocyte as priming template, these extracts show a spontaneous *de-novo* formation of ordered arrays of cell-like compartments without a membrane envelope (abbreviated as 'protocells' hereafter). Protocells with typical radii of some 100 μm emerge spontaneously within about 30 min (see Fig. 1 for an example), even though the extract is arrested in interphase with a chemically abolished protein synthesis and despite a lack of chromatin that could serve as nucleation seed. This spontaneous and dynamic compartmentalization process is a genuine non-equilibrium phenomenon that is disrupted by ATP/GTP depletion, or by blocking the microtubule cytoskeleton dynamics or dynein motors; blocking actomyosin or kinesin motors involved in mitotic spindles had little to no effect (Cheng and Ferrell, 2019). Albeit requiring the activity of microtubules and molecular motors, protocells are not mere microtubule arrays as they accumulate remnant vital organelles, e.g. mitochondria (Cheng and Ferrell, 2019). Notably, supplementing the assay with sperm-derived nuclei and centrosomes, also mitosis with defined nucleation seeds has been reconstituted (Afanzar et al., 2020).

Due to the similarity of protocell patterns with organized arrays of cells and cell-like entities in developmental organisms, e.g. syncytial energids (Mitchison and Field, 2019; de Carvalho et al., 2022), we have explored potentially generic aspects of space compartmentalization with this assay at a strongly reduced complexity and improved accessibility, in the absence of priming and pre-patterning template structures. In particular, we asked which geometrical features protocell patterns have, how these evolve over time, how robust these features are when the cytoskeletal dynamics is perturbed, and how one can capture the pattern with a mesoscopic model that might allow one to conclude and extrapolate on common, generic principles of self-organized space compartmentalization in other systems, e.g. in developing organisms and tissues that involve a syncytial state.

RESULTS

Protocells show a high degree of uniformity

Following previous protocols (Cheng and Ferrell, 2019), we were able to confirm the robust emergence of protocell patterns in slab-like droplets of *Xenopus* extracts (see Materials and Methods for details). Starting from homogenous droplets of freshly prepared extract, we observed the emergence of fairly regular arrays of protocell compartments within 30-50 min after sealing the sample chamber (sketched in supplementary Fig. S1) even without priming templates, chromatin assemblies, or the action of acto-myosin (see Fig. 1A,B and the associated supplementary movie 1). In line with previous observations (Cheng and Ferrell, 2019), the pattern faded and disintegrated after about 3 h, most likely due to a progressive limitation of available ATP/GTP molecules that fuel necessary active processes.

Notably, upon pattern emergence we did not observe a successive formation of individual protocells at different spatial locations. Rather, the entire pattern became visible at the same instant of time. Given that each droplet contained several hundred protocells, i.e. the droplet diameter was always much larger than individual protocells, this observation suggests a global coupling of the entire system, akin to a spinodal decomposition or Turing-pattern formation. In both of these scenarios, a critical wave length can be named that couples growing fluctuations across the entire system, eventually leading to a global onset of the formation of periodic patterns with a long-range order.

Boundary lines between protocells had a lower absorbance in bright-field images, and hence a lower density than the interior of protocells. Most likely, radially organized microtubules are responsible for the increased crowding inside protocells as they provide a means for a constant shuttling of mitochondria and other organelles to the center region via dynein motors (Cheng and Ferrell, 2019). In line with this notion, we observed radial arrays of microtubules within individual protocells, with little to no visible overlap of microtubules between neighboring compartments (see fluorescence images in supplementary Fig. S2A,B and the associated supplementary movie 3). Exploiting and highlighting the permanent radial influx, we added minute amounts of accessory tracer beads (diameter 1 μm) to freshly prepared extract droplets, that eventually accumulated in the center of protocells. The addition of these tracers was not seen to perturb protocell formation but enhanced the contrast for subsequent image analysis.

Unlike the rather large tracer beads, inert fluorescently labeled macromolecules (10 kDa FITC-coupled dextran) were almost excluded from the interior of protocells and instead accumulated at the boundaries (Fig. 1C). This exclusion of inert macromolecules from densely crowded regions is similar to observations inside living culture cells (Donth and Weiss, 2019). Due to the good contrast between bright boundary zones and dark protocell centers, an automatic segmentation of bright-field images via a Voronoi tesselation was possible (see Materials and Methods with supplementary figures S3-4 for details), facilitating a quantification of the protocells' geometry over time. A representative example for the tesselation is shown in Fig. 1D. Due to a lack of a well-defined envelope, we defined the spatial extent of each protocell to correspond to its Voronoi cell for all evaluations.

Using the tesselation approach allowed us to go beyond a qualitative visual inspection. As a first step, we analyzed the local geometry of protocells at two different time points, i.e. right after the first emergence of the pattern and 1-2 h later. To this end, we extracted individual protocell areas A, perimeters L, and vertex numbers n_v from images of different experiments and times. Accounting for varying average protocell areas, we determined normalized areas $A_n = A/\langle A \rangle$ and perimeters $L_n = L/\langle L \rangle$ by dividing out the mean values of the respective image (see supplementary Fig. S5A,B for exemplary histograms $p(A)$ and $p(L)$ before normalization). Since a Kolmogorov-Smirnov test (5% level) did not indicate significant differences of these normalized quantities between different experiments, we combined these for comparable time points into the same set and inspected their probability density functions (PDFs) $p(A_n)$, $p(L_n)$, and $p(n_v)$. In particular, no significant differences were detected between any two experiments on untreated extracts samples or extracts to which a very low amount of taxol (concentration $\leq 0.1\,\mu$M) had been added; these data were hence combined for the analysis.

In line with the visual impression of a highly regular appearance of protocells, the statistics of vertex numbers, $p(n_v)$, highlighted a predominant occurrence of hexagonal protocells with appreciable probabilities also for pentagons and heptagons (Fig. 2A); polygons with more vertices were rare. This observation suggests a (slightly) disordered hexagonal arrangement of protocells. Despite the lower complexity of the *in-vitro* system, these data are in very good agreement with earlier reports on the spatial organization of epithelial monolayers (Kaliman et al., 2021) and chemically induced aster patterns in *Phallusia* oocytes (Khetan et al., 2021).

Moreover, the PDF of normalized protocell areas and perimeters, $p(A_n)$ and $p(L_n)$, assumed narrow shapes around a peak at unity (Fig. 2B,C), i.e. protocells in each extract showed very similar areas and geometrical shapes. These results are strikingly similar to comparable quantifications on monolayers of MDCK cells that were grown on substrates of different rigidities (Kaliman et al., 2021), suggesting common principles of space compartmentalization in spite of the very different nature of these samples. Moreover, using protocell area and perimeter to define the individual geometrical compactness, $C = \frac{L^2}{4\pi A}$, revealed typical values between a circular geometry ($C = 1$) and squares ($C = 4/\pi$), see Fig. 2D. It is worth emphasizing at this point that all of these PDFs were independent of the time point at which they were acquired (cf. blue histograms vs. symbols in Fig. 2), indicating a stable and well-organized pattern of convex compartments with rather uniform geometrical properties at all times.

Altering microtubule dynamics maintains the pattern but changes its length scale

Since protocell formation goes hand in hand with a focussing of microtubules into organized structures (Cheng and Ferrell, 2019), we reasoned that stabilizing these cytoskeletal filaments may affect the protocell pattern. Since taxol had been described to stabilize microtubules without inducing major changes to cytoskeletal arrangements (Verde et al., 1991), we supplemented fresh extracts with this anti-cancer drug at different concentrations (see Materials and Methods). As a result, we observed that an increasing taxol concentration (here tested up to 2 μM) led to patterns with decreasing protocell sizes (see Fig. 3A for example images). Confocal fluorescence imaging also revealed that microtubule arrays with a radial symmetry were still formed in the presence of taxol, albeit appearing slightly less tidy and, due to the stabilizing action of taxol, being visible already at the earliest time point at which imaging was possible (see supplementary Fig. S2C,D and the associated supplementary movie 4).

Quantifying the average protocell area $\langle A_{80} \rangle$, found 70-90 min after starting the experiment, confirmed this visual impression: A successive reduction of $\langle A_{80} \rangle$ was observed for increasing taxol concentrations (Fig. 3B). Similar observations have been reported for

microtubule asters in intact *Phallusia* oocytes (Khetan et al., 2021), suggesting that the minimalistic *in-vitro* system captures generic aspects of a self-organized spatial organization.

Quantifying the statistics of vertex number, areas, and perimeters via $p(n_v)$, $p(A_n)$, and $p(L_n)$ in the presence of taxol did not reveal marked changes, irrespective of evaluating images right after the emergence of the pattern or 1-2 h later: The mean average fractions $\langle\phi\rangle$ of pentagons, hexagons and heptagons was virtually unaltered (Fig. 3C), and the PDFs $p(A_n)$ and $p(L_n)$ for high taxol concentrations assumed the same shapes as the data shown in Fig. 2 (see supplementary Fig. S5C,D). Thus, taxol treatment maintained all geometrical features of the pattern and only reduced the intrinsic length scale of protocells.

Protocell pattern dynamics coincides with that of two-dimensional foams

To gain insights into the dynamics of protocell patterns, we monitored the average protocell area $\langle A\rangle$ as a function of time for varying taxol concentrations. In all cases, we observed a roughly linear growth, $\langle A\rangle \approx \gamma t$, albeit with variations in the growth rate γ (see Fig. 4A for representative examples). Since the area of the extract droplet was conserved, an equivalent but alternative signature of this is a power-law decrease $\sim 1/t$ of the number of protocells (cf. supplementary Fig. S6A). The observed growth in area was mainly due to merging events of protocells (see supplementary movie 2 and Fig. S6B), i.e. due to a coarsening of the pattern.

Our experimental results therefore reveal that protocell patterns feature the same statistical scale invariance as two-dimensional foams (Saint-Jalmes, 2006): Irrespective of any taxol treatment, the PDF of normalized areas, $p(A_n)$, is narrow and assumes a time-independent shape with the average protocell area growing linearly in time while coarse-graining proceeds at a conserved total area.

Moreover, despite some fluctuations of the growth rates of individual assays at the same taxol concentration, the mean growth rate $\langle\gamma\rangle$ shows a clear decrease for increasing amounts of taxol in the investigated concentration range (Fig. 4B). Therefore, the typical time scales for pattern coarse-graining becomes successively larger when the dynamics of microtubules is compromised by taxol addition.

Long-range order of protocell patterns

Aiming at exploring the spatial arrangement of the observed pattern on intermediate length scales, we next probed the correlation of areas of neighboring protocells. To this end, we first determined for each cell (labeled by an index i) all next-neighbor (NN) cells (labeled with j) that share a common edge. For these, we defined a NN correlation function of area fluctuations,

$$g_i = \left\langle \left(A_i - \langle A \rangle \right) \left(A_j - \langle A \rangle \right) / < A >^2 \right\rangle_{j \in \mathrm{NN}(i)} . \quad (1)$$

Given that the PDF of protocell areas was fairly narrow, the PDF of correlation values, $p(g)$ can be expected to be narrow and symmetric around a peak at zero if protocells assume a spatially ordered arrangement. Pooling again experiments at comparable time points right after pattern emergence and 1-2 h later, we observed that $p(g)$ was indeed quite narrow with only a small skewness (Fig. 5A). Without a comparison to mathematical models, however, a proper rating whether the observed skewness is to be deemed large or small is impossible at this point.

To obtain a more significant, self-contained measure for the spatial arrangement of protocells, we inspected the variance of protocell centers encountered within a circle of radius R around randomly chosen points in the extract. For growing radii, more and more protocells will be within such a circle, yet fluctuations of the actually encountered number will very much depend on the pattern's large-scale organization. Denoting by μ and σ^2 the mean and variance of the number of center points found within a test circle of radius R, the normalized number variance $\Sigma_2(R) = \sigma^2 / \mu$ is indeed a sensitive measure for spatial order: For simple Poissonian random point patterns, Σ_2 remains at unity for increasing radii, hence highlighting strong spatial fluctuations. In contrast, a strictly hexagonal point pattern yields an oscillatory decay of Σ_2 to zero for increasing radii (cf. also Discussion). In fact, patterns for which Σ_2 approaches zero for increasing R are called hyperuniform and have recently gained considerable interest (Torquato, 2018). While strictly periodic systems are, somewhat trivially, hyperuniform, also a wide class of systems with a disordered hyperuniformity has been found (Torquato, 2018). These lack the characteristic oscillations of the normalized

number variance for increasing values of R but Σ_2 still approaches zero for large radii, indicating a long-range but non-crystalline order. Given the high degree of organization observed in protocell arrays and epithelia, suggestive of hexagonal arrays, one might hypothesize that space allocation in biology strives for (disordered) hyperuniformity. This hypothesis is even reinforced by observations of hyperuniformity in avian photoreceptor patterns (Jiao et al., 2014) as well as the jamming transition in vertebrate axis elongation (Mongera et al., 2018), since jamming phenomena are linked to hyperuniformity (Atkinson et al., 2016). The similarity of protocell patterns to two-dimensional foams, found in the previous section, leaves this aspect open since foams can feature both, a long-range order with signatures of disordered hyperuniformity (Ricouvier et al., 2019) but also a non-hyperuniform random pattern (Chieco and Durian, 2021).

We therefore probed protocell patterns on this aspect via the normalized number variance of protocell centers, $\Sigma_2(R)$. For hyperuniform systems, $\Sigma_2(R)$ should monotonously decrease for increasing test radii, R. The experimental data showed, however, a rapid and clear saturation at $\Sigma_2 \approx 0.3$, right after the onset of pattern formation and also 1-2 h later (Fig. 5B). This indicates that protocell patterns are not hyperuniform at any time point, even though a visual inspection may have suggested a near-crystalline order. Assuming values $\Sigma_2(R) < 1$, the pattern can be viewed instead to have gross geometric properties of a hard-sphere fluid (Torquato, 2018).

DISCUSSION

Summarizing our experimental results, we have found striking geometrical features in a minimalistic *in-vitro* assay that exhibits a spontaneous spatial compartmentalization: The observed pattern of protocells is characterized by narrow distributions of vertex numbers, areas, and perimeters (Fig. 2) with a characteristic length scale that is tunable by the addition of the microtubule-directed drug taxol (Fig. 3). The pattern shows dynamic coarse-graining features like a two-dimensional foam (Fig. 4) without a long-range ordering (Fig. 5). Notably, coarse-graining preserves the pattern geometry, i.e. protocells show self-similar arrangements over time. Given that the observed phenomena compare favorably to previous observations in *Phallusia* oocytes (Khetan et al., 2021), *Drosophila* syncytial blastoderms (de Carvalho et al., 2022), and even culture cell monolayers (Kaliman et al., 2021), it is tempting to hypothesize

common generic principles of a dynamic space compartmentalization, e.g. similar force fields and optimization functionals, upon which organism-specific features may be superimposed.

To follow up on this idea and to rationalize our experimental findings, we have formulated two simple and generic statistical models of how protocell centers attain their spatial arrangement, hence allowing for a comparison with the geometrical features of protocell patterns. As a reasonable baseline, we also considered a Poisson random point pattern (PRP), which is supposedly the most simple process of distributing center points in the plane (see Fig. 6A for a visualization). To formulate these two models, we took the following experimental observations as an input: Protocell patterns were seen to emerge spontaneously all over the droplet by radially arranging microtubules that supported an accumulation of organelles at the center. Despite a slow coarsening, all geometric features of the patterns were maintained over time. Albeit the protocell pattern did not emerge from a single point, as also mentioned in Ref. (Cheng and Ferrell, 2019), we have assumed for simplicity only point-like seeds for the model, representing the centers of the initial protocell structures. Therefore, we neglected at first instance any coarse-graining dynamics and assumed an instantaneous existence of N center points (seeds) that are placed on the unit square, hence defining a typical length scale $\lambda = \sqrt{2/\left(\sqrt{3}N\right)}$ (chosen in accordance with (Zhu et al., 2001)). Using a tunable parameter $\alpha \in [0, 0.7]$, two-dimensional point patterns were created in both models with the following rules (cf. sketches in Fig. 6B,C):

1. Cell centers are chosen randomly from the unit square with the constraint that the minimal distance to neighboring centers is at least $\alpha\lambda$.
2. Cell centers are created by displacing vertices of a triangular lattice by a distance $\xi\lambda$ in a random direction, with $\xi \in [0, \alpha]$ being a uniformly distributed random number.

Both schemes yield the steady-state pattern when protocells emerge simultaneously, grow over time and stop growing upon contact. Stop of growth upon contact reflects that coarse-graining, i.e. a fusion of neighboring units, is not considered (see below for a dynamic extension). In model 1, random seed positions are combined with a uniform and isotropic growth rate, whereas model 2 assumes hexagonal cells (due to a global instability of the uniform state with a defined wave vector, like in Turing-pattern formation or spinodal

decomposition), perturbed by spatiotemporal fluctuations of the growth rate. The two models therefore reflect very different ways of how the pattern emerges (local vs. global onset).

Albeit not apparent immediately, the models feature very different long-range organization: PRPs are characterized by a strong randomness and hence the normalized number variance remains unity for all test radii R, whereas for $\alpha \approx 0.5$ both, model 1 and model 2 deviate from unity for large radii (Fig. 6D). While model 1 displays a geometry that complies with a hard-disk fluid, indicated by $\Sigma_2 \to const. < 1$ for large radii (Torquato, 2018), model 2 bears a resemblance to hexagonal patterns and features an ever-decreasing number variance ($\Sigma_2 \to 0$) as expected for systems with disordered hyperuniformity (Torquato, 2018).

Using $N = 1000$ center points (for comparability with experiments), we produced $M = 50$ different realizations for each model and different choices of α. These point patterns were subjected to a Voronoi tesselation and evaluations of PDFs was done as for the experimental data. As a result, we observed that model 1 and model 2 lead to a very good agreement with the experimental data when choosing $\alpha_1 = 0.55$ and $\alpha_2 = 0.45$, respectively, while PRPs were inconsistent with the experimental data. In particular, PDFs for vertex number, cell area, and perimeter feature a shape that is empirically well captured by a narrow gamma distribution (Zhu et al., 2001), and all PDFs of models 1 and 2 match the experimental data so well that one cannot really claim a superiority of one, even though the compactness yields a first hint that model 1 might describe the experimental data somewhat better (see Fig. 2).

In line with this hint, the PDF of next-neighbor correlations of protocells provides further evidence for model 1 being the more adequate description (see Fig. 5A). Finally, the normalized number variance Σ_2 of model 1 captures the experimental data well, whereas the hyperuniform model 2 shows marked deviations (Fig. 5B). Again, data for PRPs are inconsistent with the experimental data. As a formal caveat, we note here that only an asymptotic vanishing of $\Sigma_2(R)$ can properly reveal hyperuniformity, i.e. the finite sample size and potential inhomogeneities of protocell densities might mask asymptotic hyperuniform signatures (Dreyfus et al., 2015).

Since model 1 captures all geometrical features of protocell patterns, we have implemented a dynamic coarse-graining of these point patterns as a next step. In line with experiments, we demanded a conservation of the total area of the pattern, i.e. in each time

step only a single fusion event of an existing cell with a neighboring cell was allowed, leading to a slow linear increase of the mean cell area. Reasoning that close neighbors have an elevated probability to fuse (see next paragraphs for discussion), we determined at each step for all available points of the pattern the respective nearest neighbor. From this set of pairs we considered only the one-third subset of smallest distances from which we randomly selected one pair of points for fusion (combining them into a single new point located half-way between the original points). With this approach, small distances between neighbors are favored without enforcing fusion events to always invoke the smallest cells and distances. As a result, we observed that this simple, area-preserving dynamics resulted in very similar statistics before and after coarse-graining (see supplementary Fig. S7 for an example), i.e. the self-similarity of the pattern was preserved, in agreement with our experimental observations.

Based on the very good matching of our experimental data with model 1 (even after applying a simple coarse-graining dynamics), we will narrow down the emergence of protocell patterns to the following set of rules: (i) Protocell seeds emerge simultaneously at almost final positions. (ii) These seeds grow in an isotropic fashion at very similar growth rates by radial uptake of material from the close vicinity until touching neighboring protocells. (iii) At this stage, growth stops and protocells repell each other sufficiently strong to not fuse immediately, i.e. a quasi-stationary, frustrated state of the pattern is reached. (iv) Then, fusion events of close neighbors will lead to a slow coarse-graining without altering the geometry, i.e. a pattern with scale-invariant properties is maintained.

These somewhat abstract rules may be put into the biological context as follows. Protocell formation requires the spatiotemporal organization of microtubules into arrays with radial symmetry that serve as the defining mechanical structure and as a means for an inwards transport of material. Therefore, their spontaneous emergence can be related to rule (i): Similar to artificial systems made from purified components (Nedelec et al., 1997; Surrey et al., 2001; Roostalu et al., 2018), the initially well-mixed extract will start polymerizing microtubules that interact via (multi-headed) motors when reaching a critical length and overlap. As a result, microtubules (or microtubular bundles) will try to focus into radial arrays at all positions in the assay. Since all loci in the extract have the same, supposedly low, kinetic barrier for microtubule formation, fluctuations will eventually determine where these structures will emerge, akin to fluctuation-induced nucleation in oversaturated solutions. Radially organized microtubule structures will hence form at about the same time at random positions. Once established, they recruit material to their centers, e.g. organelles, hence creating protocell seeds as requested in rule (i). Uptake of more

material and inwards transport along microtubules let protocells grow at the center of the structures, which is in accordance with rule (ii). When neighboring protocells have grown large enough that they are prone to touching, competition for the same local pool of material needs to be considered as it might be a limiting factor. Moreover, without the action of an appropriate subset of (multi-headed) motors and a sufficient overlap of the two microtubule arrays, neighboring microtubule arrays will entropically repell each other like soft balls (Nedelec, 2002), leading to a mechanically frustrated pattern, in accordance with rule (iii). Please note that a comparable aster repulsion has recently been seen in the *Drosophila* syncytial blastoderm (de Carvalho et al., 2022).

Subsequent coarse-graining can take place if two neighboring arrays occasionally have a sufficient overlap and an appropriate subset of (multi-headed) motors for driving a fusion event (see (Nedelec, 2002; Roostalu et al., 2018) for detailed simulations). This slow coarse-graining by fusion corresponds to rule (iv), in which the assumption that close neighbors can fuse easiest (but also randomly) is based on the fact that a proper mutual configuration is needed for an attractive interaction. Given the still considerable complexity of our assays and our current lack of sufficient knowledge on the interaction between microtubule arrays in protocells, we need to defer the implementation of a more refined dynamic model, beyond the statistical model 1 with its simplified coarse-graining dynamics, to future work.

The observed effect of taxol addition, i.e. a decreasing length scale of the pattern, is most likely rooted in a reduced fraction of long microtubules due to a taxol-induced suppression of microtubule dynamics (Yvon et al., 1999): In untreated extracts, a lack of translation leads to a limited pool of tubulin and/or microtubule-associated proteins (Ishihara et al., 2021), i.e. the dynamical instability will lead to an outcompetition of small and shrinking microtubules by long and growing filaments. Hence, remaining microtubules grow longer on the expense of unsuccessful smaller ones that eventually vanish. Stabilizing all seeds by taxol increases the amount of growing filaments that compete for the same pool while growing with similar kinetics, eventually resulting in more but shorter filaments, that may consist of single microtubules or bundles (Ishihara et al., 2021). In support of this reasoning, we observed that the ratio ζ of short versus long microtubules, as extracted from fluorescence images (see Materials and Methods), increased from $\zeta \approx 4.25$ in untreated extracts to an average of $\zeta \approx 9.54$ in extracts treated with 1 μM taxol (see Materials and

Methods). Fluorescence imaging of protocells in the presence of taxol also indicates shortened microtubules (see Fig. S2C,D in comparison to Fig. S2A,B).

Stabilization and shortening of microtubules (or bundles) due to taxol also nicely fits the discussion in the previous paragraphs: Stabilizing microtubules in the initial phase results in smaller radial structures, i.e. the frustrated, quasi-stationary state prior to coarse-graining will feature more but smaller protocells. Since only the filament length scale but not the rules of interaction have been changed, the pattern maintains the same geometrical properties as in untreated extracts. Moreover, taxol hampers the dynamic instability of microtubules and hence their ability to explore adjacent regions, so that achieving sufficient microtubule overlaps between neighboring protocells for fusion events will require more time. As a consequence, lower coarse-graining rates γ are expected in the presence of taxol, in line with our experimental observation.

The protocell patterns observed here are not only similar to aster arrays in *Phallusia* oocytes (Khetan et al., 2021) and the *Drosophila* syncytial blastoderm (de Carvalho et al., 2022), but also to epithelial cell monolayers (Kaliman et al., 2021). Based on the phenotypical similarities, we speculate that these diverse systems share common principles for their space compartmentalization that are most likely rooted in fairly simple mechanical cues. While this hypothesis suggests itself when considering aster arrays without an envelope, e.g. energids in a syncytium state, the relation to developing tissues is somewhat less straightforward as it invokes successive divisions of membrane-enveloped cells, rather than spontaneous protocell formation and fusion events. Nevertheless, an initially random placement of cells (cf. rule (i)) and an intermediate frustrated arrangement of them in an emerging tissue due to competition for space (cf. rule (iii)), is conceivable: Cells are small and hence are subject to thermal and active fluctuations that perturb cell division axes and cleavage planes, leading to a certain randomness in cell positions and sizes. Adhesion will keep cells together, maybe even with perfect wetting angles as suggested for a developing retina (Hayashi and Carthew, 2004), but cells will also exert mutual repulsive forces to maintain their individual volumes and positions, potentially blocking each other's motion. As a result, a mechanically frustrated pattern of cells with all properties of a random-packing process of soft spheres may emerge and hence key features of model 1, discussed above, are met. In fact, modeling cells as simple soft-repulsive balls that force each other into positions of least constraints has been surprisingly successful in predicting cell positions in the early embryogenesis of *C. elegans* (Fickentscher et al., 2013; 2016). Since cell division is typically

much slower than local shape adaptions, similar to slow protocell fusion in our assay, the random-packing geometry can be expected to be preserved for long periods. Successive cell divisions could even be interpreted as a time-reversed coarse-graining dynamics that maintains geometric features of the pattern.

In view of our findings and interpretations, it will be interesting to quantitatively explore which self-organizing patterns of asters, energids, cells, and (embryonic) tissues comply with the idea of a random-packing process with conserved geometric properties, and whether such patterns eventually do reach a (disordered) hyperuniform ordering. Our present data suggest that hexagonal patterns with a long-range ordering could be a very rare and supposedly special case of space compartmentalization, i.e. an organization based on random seeds might be the standard case. It is also worth noting that all of the aforementioned pattern formation happens far from thermal equilibrium and most likely relies on mechanically driven self-organization and adaption processes (rather than a self-assembly and relaxation towards equilibrium states with minimal free energy). Supposedly, not only ATP-fueled deterministic forces are key to the pattern emergence but also the ambient non-equilibrium noise that arises by the plethora of nucleotide hydrolysis events. In fact, a variety of stationary states only emerges due to multiplicative noise far from equilibrium (see (Garcia-Ojalvo and Sancho, 1999) for an introduction). Therefore, minimal *in-vitro* assays, like the one used here, are valuable tools that can help to reduce the daunting complexity of living matter and to reveal putative common principles for a wider class of systems.

MATERIALS AND METHODS

Interphase extract preparation

The interphase extract preparation protocol was adapted from Refs. (Deming and Kornbluth, 2006) and (Sparks and Walter, 2018) with minor modifications (see supplement for a list of important reagents and their abbreviations): A single HCG injection 16-17 h before the experiment was sufficient to obtain proper egg harvest. We changed the concentration of Marc's Modified Ringer's (MMR) to 0.5x (instead of 0.25x) and washed five times instead of three times. Correcting for a typo, we used KCl instead of HCl in the egg lysis buffer (ELB) preparation. Cycloheximide was added to the extract only after egg crushing (not in the ELB) but cytochalasin B was added already to the ELB in the centrifuge tube to which eggs were transfered for crushing ($50\,\mu$g /mL final concentration).

Interphase-arrested cytoplasmic extracts were prepared from freshly laid eggs of *Xenopus laevis* following standard protocols (Deming and Kornbluth, 2006; Sparks and Walter, 2018). In brief, eggs in the metaphase stage of meiosis II were collected and dejellied. These eggs were washed first with 0.5x MMR, then with ELB containing DTT, and finally packed by centrifugation with the excess buffer being removed. Packed eggs were crushed and fractionated into three distinctive layers by centrifugation using a Beckman Coulter JS-13.1 swinging bucket rotor and open-top polyclear centrifuge tubes (Seton, 4/6.5 mL). Then the mid cytoplasmic layer was carefully isolated and supplemented with 5 μg/mL of aprotinin, 5 μg/mL of leupeptin, 5 μg/mL of cytochalasin B, 50 μg/mL of cycloheximide, and stored on ice; these extracts were used within 10 h. The addition of cycloheximide inhibits protein synthesis, including the synthesis of new cyclin. Thus, the extract is arrested in an interphase state. The addition of protease inhibitors (aprotinin, leupeptin) limits protein degradation (Chan and Forbes, 2006), while cytochalasin B suppresses actin polymerization (MacLean-Fletcher, 1980). Some extracts were also supplemented with taxol to enhance microtubule stabilization without inducing major changes to cytoskeletal arrangements (Verde et al., 1991).

Sample preparation and imaging

For imaging, interphase extract was supplemented with 1 μm polystyrene beads (1% by volume of stock solution) and FITC-Dextran (1% by volume of stock solution). Not adding any of these resulted in the same pattern formation but the contrast of protocell centers to the periphery was considerably dimmer. DMSO concentrations of all extracts were maintained at 1% by volume, if needed by compensating with pure DMSO to limit the influence of microtubule stabilization by DMSO (Wignall and Heald, 2001). Extracts were mixed by gentle flickering, pipetting 3-4 times with a cut-off tip and carefully inverting the tube.

Fluorinated ethylene propylene (FEP) tapes were used to cover the bottom microscope slide and top glass cover slip that were separated by a 120 μm double-side tape spacer into which circular 9 mm holes were punched for hosting the extract droplets (see supplementary Fig. S1A); FEP coating was done one day before the experiment. To each of the holes, 4 μL of the extract was carefully pipetted into the center. Then, the whole chamber was sealed immediately with the coverslip to avoid evaporation. These samples were imaged with one of the following two microscopes in a tile-scan mode: a Leica

DMI6000B inverted microscope with an HC PLS-APO 10x/0.30 DRY objective and a Leica DFC360FX camera or a Leica SP5 II confocal laser scanning microscope with a HCX PL APO CS 10x/0.40 DRY UV objective with 3.03 μm pixel width (512×512 pixel tiles) and open pinhole. In both cases bright-field images were recorded, with an additional fluorescence channel on the SP5 for detecting FITC-Dextran (Excitation: 496 nm, Emission: 511-550 nm). The extract was imaged for more than four hours at room temperature (20 °C) with a minimal time interval between consecutive tile scans.

For imaging of microtubules, rhodamine-labeled tubulin was first resuspended in 1 μL of 1 mM GTP-containing general tubulin buffer and 8 μL of fresh interphase extract. Samples for imaging were subsequently prepared by mixing 3 μL of this solution to 50 μL premixed interphase extract, hosted by a modified sample chamber for high-resolution imaging (see supplementary Fig. S1B). Fluorescence imaging was performed with a Leica SP5 II confocal laser scanning microscope, using an excitation wavelength of 561 nm and a detection range of 575-650 nm. Images (512×512 pixels, pixel size chosen according to Nyquist's theorem) were acquired with mono-directional scanning (scan frequency 400 Hz) within a maximum period of two hours, using a HCPL APO 100x/1.40 OIL or a HCXPL APO 63x/1.4 OIL CS2 objective.

Image analysis and pattern detection

As a first step, shading correction and merging of images from a tile scan was performed with the Leica LAS X software using the options auto-stitching, smoothing, and linear blending, taking only the bright-field channel as a reference. Images from the Leica DMI6000B were resized by a factor 1/4 in each direction to arrive at a pixel dimension of 3 μm/px for all microscopes.

Using the time series of these reconstructed large-field images, the start and end times between which protocells were visible was determined visually for each droplet preparation. For these periods, the following operations were performed on the large-field images (see also supplementary Fig. S3 for illustration):

- Manual marking of the droplet boundary, defining a rectangular region of interest in each image for further processing.
- Automatic segmentation of the droplet boundary by detecting the ring of darkest pixels that is present at the droplet border.
- Binarization of the droplet image using the lowest of two thresholds that are

obtained by Otsu's method (three-pixel classes with minimal intra-class variance, implemented via the *multithresh* function in Matlab).

Subsequently, further filtering was performed to achieve a single-connected component of dark pixels within each protocell, defining the cell center. To this end, a sequence of classic morphological operations was applied (see supplementary Fig. S4 for illustration): Hole-filling (connectivity: four), image opening (using a 3×3 square), image dilation, hole-filling, and image erosion, with the same structural elements as before. Finally, connected sets of center pixels (highlighted in blue in Fig. S4D) were filtered according to their area histogram (using a bin width according to Scott's rule, connectivity for area: eight), i.e. the areas within the first histogram bin were rated as erratic pixels and hence removed (cf. examples before and after in Fig. S4D,E). The centroid positions of these filtered connected components were then used for a Voronoi tessellation (Fig. S4F).

For the quantitative analyses in Figs. 2 and 5 we have used the data from five large droplets from different repeats of the assay, yielding a total of 9971 protocells (right after at the first emergence of the pattern). The average number of 2000 protocells per droplet provided sufficient statistics also for long-range measures like Σ_2. While smaller droplets were insufficient for this (and were hence not included), their local measures were in full agreement with the results shown in Fig. 2. For high-taxol conditions (supplementary Fig. S5), we have used three large droplets with an initial number of 10049 protocells. Due to the progressive coarse-graining, statistics for later time points (1-2 h after pattern emergence) relied on about 50% of the initial number of protocells. Since data shown in Figs. 3,4 only report on local measures, we have considered here a total of 13 droplet repeats, i.e. several thousand protocells were available for determining areas and vertex numbers at each indicated taxol concentration.

Taxol-induced change of the fraction of long microtubules

To extract microtubule lengths from fluorescence images, we used SOAX, a freely available analysis software for biopolymer networks (Xu et al., 2015). Since very short filaments in semi-dilute and dense systems are difficult to assess with light microscopy without missing significant portions of this pool (unless fluorescent filaments are very sparse), we only considered microtubules with a length of at least $5\,\mu$m. From all detected microtubules of all images (see supplementary Fig. S8 for examples), we calculated the fraction of filaments

with a length smaller than 20 μm, f_s, and the complementary fraction of longer filaments, f_ℓ. The ratio $\zeta = f_s / f_\ell$ was taken as a self-normalizing measure for the frequency of long microtubules. From two replicates per condition, we obtained $\zeta_1 = 4.06$ and $\zeta_2 = 4.46$ (without taxol) and $\zeta_1 = 11.5$ and $\zeta_2 = 8.14$ (1 μM taxol). Using $|\zeta_1 - \zeta_2| / \left(2\langle\zeta\rangle\right)$ for the relative error, this resulted in an average ratio $\langle\zeta\rangle 4.25 \pm 5\%$ without taxol versus $\langle\zeta\rangle 9.54 \pm 17\%$ at 1 μM taxol. Thus, the fraction of shorter filaments was significantlt increased in the presence of taxol. We also would like to note that it is likely that long filaments actually consist of microtubule bundles that may emerge by an autocatalytic growth of individual microtubules to a mean length of about 16 μm (Ishihara et al., 2021).

Acknowledgements

We thank A.C. Ramos and O. Stemmann (University of Bayreuth, Genetics) for providing Xenopus eggs, and A. Hanold for supporting the extract preparation.

Competing interests

No competing interests.

Contribution

Insert the Contribution text here.

Funding

Financial support by the VolkswagenStiftung (Az. 92738) and by the EliteNetwork of Bavaria (Study Program Biological Physics) are gratefully acknowledged.

Data availability

Data presented in this study are available from the corresponding author upon reasonable request.

Supplementary

See supplementary figures in a separate PDF and movies.

References

Afanzar, O., Buss, G., Stearns, T. and Ferrell, J. (2020). The nucleus serves as the pacemaker for the cell cycle. *Elife* **9**, e59989.

Atkinson, S., Zhang, G., Hopkins, A. and Torquato, S. (2016). Critical slowing down and hyperuniformity on approach to jamming. *Phys Rev E* **94**, 012902.

Chan, R. C. and Forbes, D. J. (2006). In vitro study of nuclear assembly and nuclear import using Xenopus egg extracts. In *Xenopus Protocols*. Humana Press, pages 289–300.

Cheng, X. and Ferrell, J. (2019). Spontaneous emergence of cell-like organization in Xenopus egg extracts. *Science* **366**, 631–637.

Chieco, A. and Durian, D. J. (2021). Quantifying the long-range structure of foams and other cellular patterns with hyperuniformity disorder length spectroscopy. *Phys Rev E* **103**, 062609.

Classen, A.-K., Anderson, K., Marois, E. and Eaton, S. (2005). Hexagonal packing of drosophila wing epithelial cells by the planar cell polarity pathway. *Dev Cell* **9**, 805–817.

de Carvalho, J., Tlili, S., Hufnagel, L., Saunders, T. and Telley, I. (2022). Aster repulsion drives short-ranged ordering in the drosophila syncytial blastoderm. *Development* **149**, dev199997.

Deming, P. and Kornbluth, S. (2006). Study of apoptosis in vitro using the Xenopus egg extract reconstitution system. In *Xenopus Protocols*. Humana Press, pages 379–393.

Donth, C. and Weiss, M. (2019). Quantitative assessment of the spatial crowding heterogeneity in cellular fluids. *Phys. Rev. E* **99**, 052415.

Dreyfus, R., Xu, Y., Still, T., Hough, L., Yodh, A. and Torquato, S. (2015). Diagnosing hyperuniformity in two-dimensional, disordered, jammed packings of soft spheres. *Phys. Rev. E* **91**, 012302.

Fickentscher, R., Struntz, P. and Weiss, M. (2013). Mechanical cues in the early embryogenesis of caenorhabditis elegans. *Biophys J* **105**, 1805–1811.

Fickentscher, R., Struntz, P. and Weiss, M. (2016). Setting the clock for fail-safe early embryogenesis. *Phys Rev Lett* **117**, 188101.

Franze, K. (2020). Integrating chemistry and mechanics: The forces driving axon growth. *Ann. Rev. Cell Dev. Biol.* **36**, 61–83.

Garcia-Ojalvo, J. and Sancho, J. M. (1999). *Noise in Spatially Extended Systems*. Institute for Nonlinear Sciences. Springer New York, NY.

Goehring, N., Trong, P., Bois, J., Chowdhury, D., Nicola, E., Hyman, A. and Grill, S. (2011). Polarization of par proteins by advective triggering of a pattern-forming system. *Science* **334**, 1137–41.

Good, M. C., Vahey, M. D., Skandarajah, A., Fletcher, D. A. and Heald, R. (2013). Cytoplasmic volume modulates spindle size during embryogenesis. *Science* **342**, 856–60.

Gross, P., Kumar, K., Goehring, N., Bois, J., Hoege, C., Julicher, F. and Grill, S. W. (2019). Guiding self-organized pattern formation in cell polarity establishment. *Nat Phys* **15**, 293–300.

Guignard, L., Fiuza, U.-M., Leggio, B., Laussu, J., Faure, E., Michelin, G., Biasuz, K., Hufnagel, L., Malandain, G., Godin, C. and Lemaire, P. (2020). Contact area-dependent cell communication and the morphological invariance of ascidian embryogenesis. *Science* **369**, eaar5663.

Hayashi, T. and Carthew, R. (2004). Surface mechanics mediate pattern formation in the developing retina. *Nature* **431**, 647–652.

Ishihara, K., Decker, F., Caldas, P., Pelletier, J., Loose, M., Brugues, J. and Mitchison, T. (2021). Spatial variation of microtubule depolymerization in large asters. *Mol Biol Cell* **32**, 869–879.

Jiao, Y., Lau, T., Hatzikirou, H., Meyer-Hermann, M., Corbo, J. and Torquato, S. (2014). Avian photoreceptor patterns represent a disordered hyperuniform solution to a multiscale packing problem. *Phys. Rev. E* **89**, 022721.

Kaliman, S., Hubert, M., Wollnik, C., Nuic, L., Vurnek, D., Gehrer, S., Lovric, J., Dudziak, D., Rehfeldt, F. and Smith, A.-S. (2021). Mechanical regulation of epithelial tissue homeostasis. *Phys. Rev. X* **11**, 031029.

Khetan, N., Pruliere, G., Hebras, C., Chenevert, J. and Athale, C. (2021). Self-organized optimal packing of kinesin-5-driven microtubule asters scales with cell size. *J Cell Sci* **134**, jcs257543.

Kondo, S. and Miura, T. (2010). Reaction-diffusion model as a framework for understanding biological pattern formation. *Science* **329**, 1616–1620.

Koser, D., Thompson, A., Foster, S., Dwivedy, A., Pillai, E., Sheridan, G., Svoboda, H., Viana, M., Costa, L., Guck, J., Holt, C. and Franze, K. (2016). Mechanosensing is critical for axon growth in the developing brain. *Nature Neuroscience* **19**, 1592–1598.

Krzic, U., Gunther, S., Saunders, T., Streichan, S. and Hufnagel, L. (2012). Multiview light-sheet microscope for rapid in toto imaging. *Nature Methods* **9**, 730–U304.

Lauschke, V., Tsiairis, C., Francois, P. and Aulehla, A. (2013). Scaling of embryonic patterning based on phase-gradient encoding. *Nature* **493**, 101–5.

MacLean-Fletcher, S. (1980). Mechanism of action of cytochalasin b on actin. *Cell* **20**, 329–341.

Mitchison, T. and Field, C. (2019). Toward synthetic cells. *Science* **366**, 569–570.

Mitchison, T., Ishihara, K., Nguyen, P. and Wühr, M. (2015). Size scaling of microtubule assemblies in early xenopus embryos. *Cold Spring Harbor Perspectives in Biology* **7**, a019182.

Mitchison, T., Wühr, M., Nguyen, P., Ishihara, K., Groen, A. and Field, C. (2012). Growth, interaction, and positioning of microtubule asters in extremely large vertebrate embryo cells. *Cytoskeleton* **69**, 738–750.

Mongera, A., Rowghanian, P., Gustafson, H., Shelton, E., Kealhofer, D., Carn, E., Serwane, F., Lucio, A., Giammona, J. and Campas, O. (2018). A fluid-to-solid jamming transition underlies vertebrate body axis elongation. *Nature* **561**, 401–405.

Nedelec, F. (2002). Computer simulations reveal motor properties generating stable antiparallel microtubule interactions. *J Cell Biol* **158**, 1005–1015.

Nedelec, F. J., Surrey, T., Maggs, A. C. and Leibler, S. (1997). Self-organization of microtubules and motors. *Nature* **389**, 305–308.

Ricouvier, J., Tabeling, P. and Yazhgur, P. (2019). Foam as a self-assembling amorphous photonic band gap material. *Proc Natl Acad Sci USA* **116**, 9202–9207.

Roostalu, J., Rickman, J., Thomas, C., Nedelec, F. and Surrey, T. (2018). Determinants of polar versus nematic organization in networks of dynamic microtubules and mitotic motors. *Cell* **175**, 796–808.

Saint-Jalmes, A. (2006). Physical chemistry in foam drainage and coarsening. *Soft Matter* **2**, 836–849.

Sonnen, K., Lauschke, V., Uraji, J., Falk, H., Petersen, Y., Funk, M., Beaupeux, M., Francois, P., Merten, C. and Aulehla, A. (2018). Modulation of phase shift between wnt and notch signaling oscillations controls mesoderm segmentation. *Cell* **172**, 1079–1090.

Sparks, J. and Walter, J. C. (2018). Extracts for analysis of DNA replication in a nucleus-free system. *Cold Spring Harbor Protocols* **2019**, 194–206.

Sugimura, K. and Ishihara, S. (2013). The mechanical anisotropy in a tissue promotes ordering in hexagonal cell packing. *Development* **140**, 4091–4101.

Surrey, T., Nedelec, F., Leibler, S. and Karsenti, E. (2001). Physical properties determining self-organization of motors and microtubules. *Science* **292**, 1167–1171.

Torquato, S. (2018). Hyperuniform states of matter. *Phys Rep* **745**, 1–95.

Turing, A. M. (1952). The chemical basis of morphogenesis. *Phil Transactions Royal Soc B* **237**, 37–72.

Verde, F., Berrez, J., Antony, C. and Karsenti, E. (1991). Taxol-induced microtubule asters in mitotic extracts of xenopus eggs: requirement for phosphorylated factors and cytoplasmic dynein. *J Cell Biol* **112**, 1177–1187.

Wignall, S. and Heald, R. (2001). Methods for the study of centrosome-independent spindle assembly in xenopus extracts. *Methods in Cell Biology* **67**, 241–256.

Xu, T., Vavylonis, D., Tsai, F.-C., Koenderink, G., Nie, W., Yusuf, E., Lee, I.-J., Wu, J.-Q. and Huang, X. (2015). Soax: A software for quantification of 3d biopolymer networks. *Sci Rep* **5**, 9081.

Yamamoto, K. and Kimura, A. (2017). An asymmetric attraction model for the diversity and robustness of cell arrangement in nematodes. *Development* **144**, 4437–4449.

Yvon, A.-M., Wadsworth, P. and Jordan, M. (1999). Taxol suppresses dynamics of individual microtubules in living human tumor cells. *Mol Biol Cell* **10**, 947–959.

Zhu, H., Thorpe, S. and Windle, A. (2001). The geometrical properties of irregular two-dimensional voronoi tessellations. *Phil Mag A* **81**, 2765–2783.

Figures

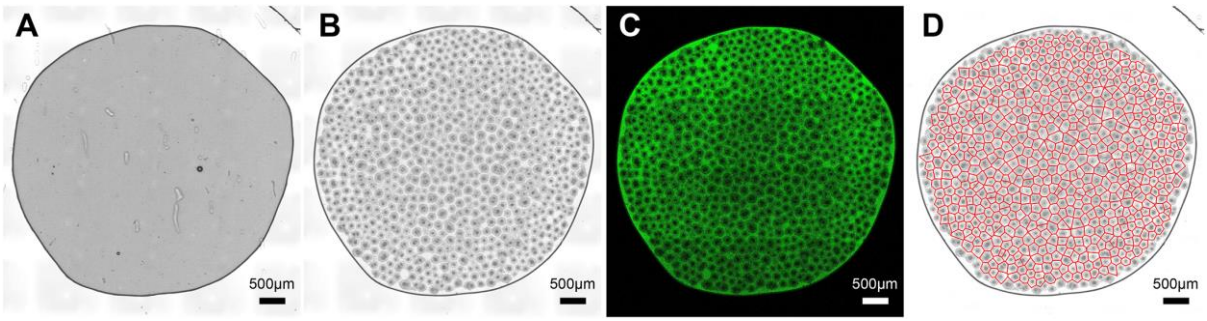

Fig. 1. Representative images of protocell pattern formation in an extract droplet. Representative bright-field images of an extract droplet (A) before and (B) after protocell formation. (C) Fluorescence imaging reveals that inert dextran molecules accumulate in boundary zones between protocells. (D) A Voronoi tesselation captures the essential geometry of the protocell pattern. Images were taken (A) 7 min and (B, C, D) 175 min after chamber loading. See supplementary movie 1 for the droplet's temporal evolution.

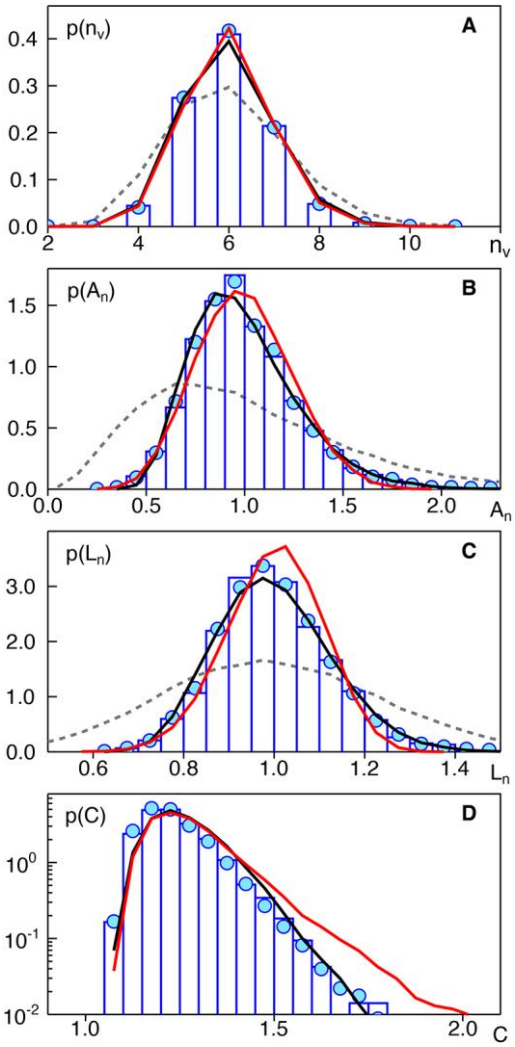

Fig. 2. Analysis of geometrical features of protocells. (A) The PDF of the vertex number, $\boldsymbol{p}(n_v)$, of protocells right after the first emergence of the pattern (blue histogram) and 1-2 h later (blue circles) is highly similar. Hexagonal cells are the most frequent phenotype, followed by appreciable amounts of pentagons and heptagons. The experimental data are well captured by model 1 ($\alpha_1 = 0.55$, black line) and model 2 ($\alpha_2 = 0.45$, red line), whereas a Poisson random point pattern (PRP), shown as grey dashed line, features marked deviations. All models are sketched in Fig. 6 and are defined in the main text. (B, C) The PDFs of normalized cell areas, $\boldsymbol{p}(A_n)$, and cell perimeters, $\boldsymbol{p}(L_n)$, feature narrow shapes and show a similar characteristics (color-code as before): Both models match the experimental data for early and late stages of the pattern, and the result for PRPs is markedly different. (D) The PDF of protocell compactness, $\boldsymbol{p}(\boldsymbol{C})$, with $\boldsymbol{C} = \dfrac{L^2}{4\pi \boldsymbol{A}}$ features a mean $\langle \boldsymbol{C} \rangle \approx 1.24$ that is

larger than the value for circles ($\boldsymbol{C}=1$) and hexagons ($\boldsymbol{C}=6/\left(\boldsymbol{\pi}\sqrt{3}\right)$) but lower than that for squares ($\boldsymbol{C}=4/\boldsymbol{\pi}$); color-code as before. The experimental data are well captured by model 1 ($\alpha_1=0.55$, black line) and slightly less good by model 2 ($\alpha_2=0.45$, red line). Please note the semilogarithmic plot style.

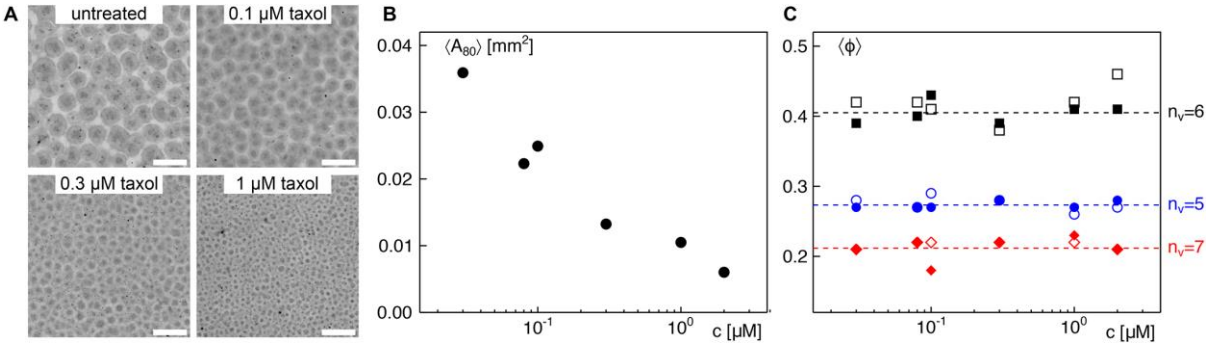

Fig. 3. Taxol addition leads to smaller protocells but does not alter the pattern geometry. (A) Representative images of protocell patterns obtained from extracts that have been supplemented with the indicated concentration of taxol; scale bars 100 $\boldsymbol{\mu}$**m**. A marked reduction of protocell sizes for increasing taxol concentrations is visible. For better visibility, the image contrast has been adjusted here; all evaluations were performed on unaltered images. (B) The average protocell area $\langle A_{80} \rangle$, found 70-90 min after starting the experiment, decreases for increasing taxol concentrations, $\boldsymbol{c}$. (C) The average fraction $\langle \phi \rangle$ of pentagonal, hexagonal, and heptagonal protocells (blue circles, black squares, and red diamonds) is almost constant for all taxol concentrations $\boldsymbol{c}$, irrespective of the time after the pattern emerged (open and filled symbols: right after pattern emergence and 1-2 h later). In addition, geometric measures like those shown in Fig. 2 remained unaltered (cf. supplementary Fig. S5A,B).

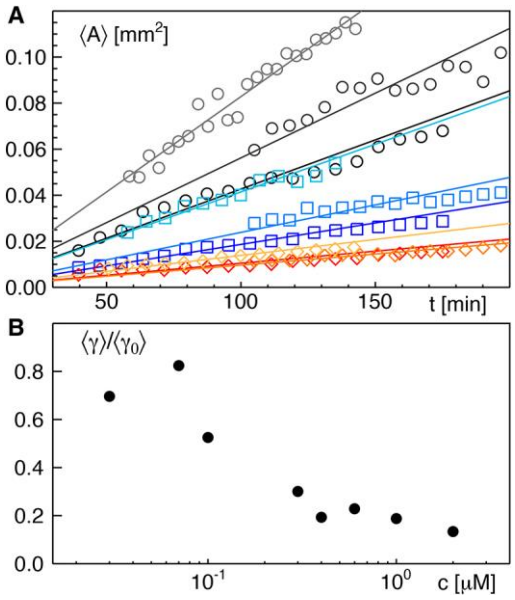

Fig. 4. Dynamic evolution of protocell patterns. (A) Representative time courses of the average protocell area, $\langle A \rangle$, for different taxol concentrations (circles, squares, diamonds for $c = 0, 0.1, 1\ \mu\mathrm{M}$; different colors indicate different repeats of the assay). All are well captured by a linear growth, $\langle A \rangle = \gamma t$, with varying growth rates γ (full lines). (B) The mean area growth rate $\langle \gamma \rangle$ decreases with increasing taxol concentrations, c, dropping down to about 15-20% of the rate observed for untreated extracts, $\langle \gamma_0 \rangle$, at 2 $\mu\mathrm{M}$.

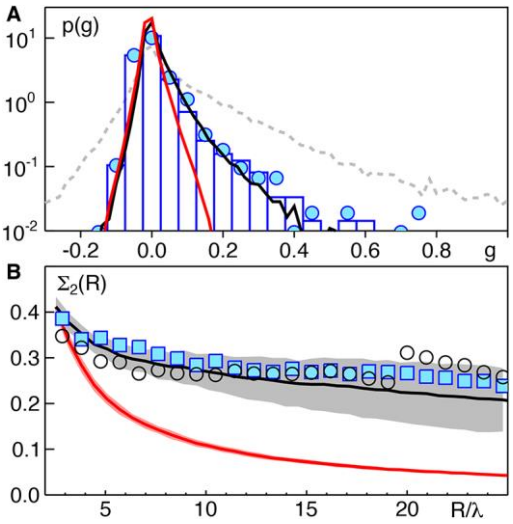

Fig. 5. Long-range organization of protocell patterns. (A) The PDF of next-neighbor area correlation values [Eq. (1)], is sharply peaked around zero for the experimental data right after the emergence of the protocell pattern (blue histogram) and after 1-2 h of coarse graining (blue circles). While model 1 captures the experimental PDF almost perfectly (black line), model 2 decays too steeply for $g > 0$ (red line); the PDF for PRPs (grey dashed line) is far too broad (B) The normalized number variance Σ_2 as a function of the rescaled test radius, R/λ, converges to a small but nonzero constant for the array of protocells (blue squares and black circles: time points right after pattern emergence and 1-2 h later, respectively). This indicates that the pattern displays no disordered hyperuniformity. While model 1 matches the experimental data well (black line) the hyperuniform characteristics of model 2 (red line) is clearly inconsistent with the experiment. Grey and red-shaded areas indicate the standard deviation for different realizations of the point patterns in the respective model.

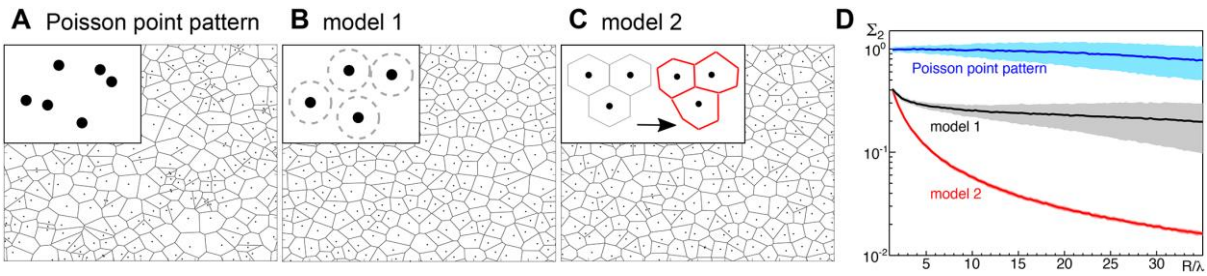

Fig. 6. Generic models used for comparison with experimental data. Voronoi tesselation for (A) a Poisson random point pattern, (B) model 1 with $\alpha = 0.55$, and (C) model 2 with $\alpha = 0.45$. Insets visualize the rules for creating the pattern of center points (see also main text for details). (D) The corresponding normalized number variances Σ_2 (shown in a semilogarithmic style) reveal that model 1 approaches a small but nonzero constant, whereas model 2 shows the typical feature of a disordered hyperuniform pattern, i.e. a decrease of Σ_2 towards zero; the Poisson random point pattern shows the anticipated behavior $\Sigma_2 \approx 1$. Shaded areas indicate the standard deviation for different realizations of the point patterns.

LIST OF IMPORTANT REAGENTS

- Human chorionic gonadotropin (Ovogest, 1000 U/mL)
- Aprotinin (Roche Diagnostics GmbH, 5 mg/mL in Milli-Q water)
- Leupeptin (Sigma-Aldrich, 10 mg/mL in Milli-Q water)
- Cytochalasin B (Calbiochem, 10 mg/mL in DMSO)
- Cycloheximide (Calbiochem, 10 mg/mL in Milli-Q water)
- Taxol (Sigma-Aldrich, 10 mg/mL stock solution in DMSO)
- 1,4-Dithiothreitol (DTT; Roche Diagnostics, 154 mg per liter of ELB)
- 1 μm polystyrene beads (Micromod Partikeltechnologie, micromer, COOH surface, product code: 01-02-103). Stock solution prepared by an aqueous 10× dilution of the pellet obtained by centrifugation.
- Fluorescein isothiocyanate-dextran (FITC-Dextran 10kDa; Sigma-Adrich). Stock solution: 10% (by weight) dissolved in Milli-Q water.
- Rhodamine labelled tubulin from bovine brain (Cytoskeleton Inc.)
- Guanosine 5'-triphosphate sodium salt hydrate (GTP; Sigma-Aldrich, 100 mM in Milli-Q water)
- General tubulin buffer: 80 mM PIPES pH 6.9, 2 mM $MgCl_2$, 0.5 mM EGTA.
- Aquapel water repellent glass treatment pack
- Egg Lysis Buffer (ELB): 250 mM sucrose, 2.5 mM $MgCl_2$, 50 mM KCl, 10 mM HEPES, pH 7.7 with KOH, 1 mM DDT.
- Dejellying solution: 2.0% (w/v) L-Cysteine (free base; Sigma-Aldrich) in Milli-Q water, pH 7.8 with KOH.
- 25x Marc's Modified Ringer's (MMR): 2.5 M NaCl, 50 mM KCl, 25 mM $MgCl_2$, 50 mM $CaCl_2$, 2.5 mM EDTA, 125 mM HEPES, pH 7.8 with NaOH.
- Secure-Seal^{TM} imaging spacers (Grace Bio-Labs, SS8X9, 8-9 mm diameter, 120 μm height)
- Fluorinated ethylene propylene adhesive film (FEP; thickness 50 μm, Holscot Europe)
- Microscope slides (Corning, plain, 25 × 75 mm, thickness 0.96-1.06 mm)
- Cover slips (Menzel Gläser, 24 × 60 mm, #1.5 thickness)

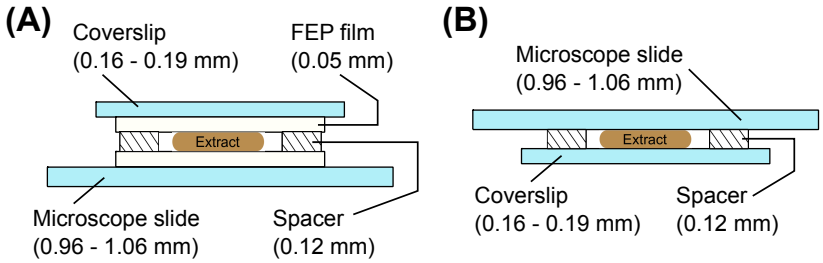

Fig. S1. Chamber design used for (A) imaging extract droplets and (B) fluorescence-imaging of microtubules (here, an aquapel-coating of the glass replaced the FEP film).

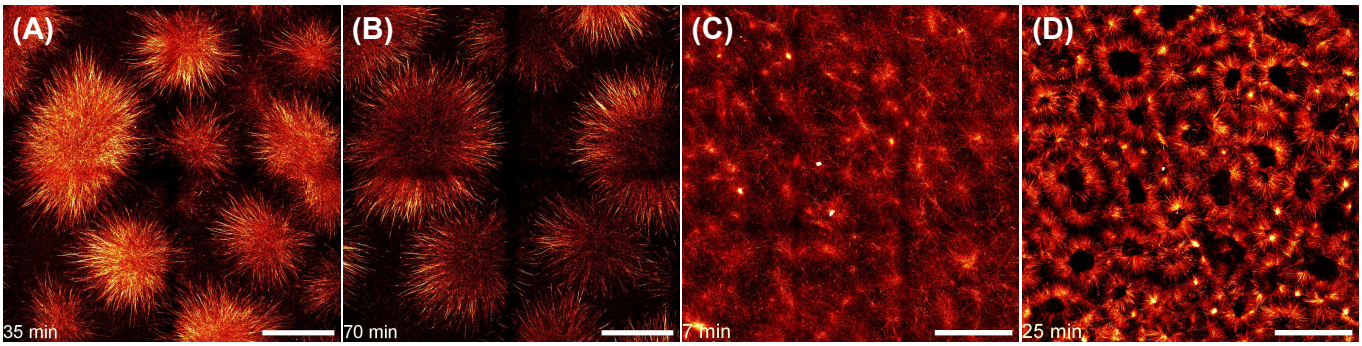

Fig. S2. Representative confocal fluorescence images of microtubules in protocells at different times of pattern evolution; scale bars 100 µm. (A) At 35 min after chamber sealing (extract without taxol), protocells feature radially arranged microtubules.(B) At 70 min, protocells still appear as radial arrays of microtubules, but with their slightly darker centers being crowded with organelles and minute amounts of polystyrene beads that are transported inwards along the radial array. (C) In the presence of 1 µM taxol, radial structures are already visible 7 min after sealing, albeit wit a less tidy organization. (D) At 25 min, these protocells still feature approximately radially arranged microtubules. Phenotypically, these protocells appear different from their counterparts in assays without taxol as microtubles seem to be solely seeded on the core (being reminiscent of eadible chestnuts). Please note the lack of microtubules in areas between protocells in all cases. Even touching protocells show little to no overlap of their individual microtubule arrays. This observation is in line with a frustrated spatial organization of protocells before the pattern undergoes a slow coarse-graining (see Discussion section in the main text).

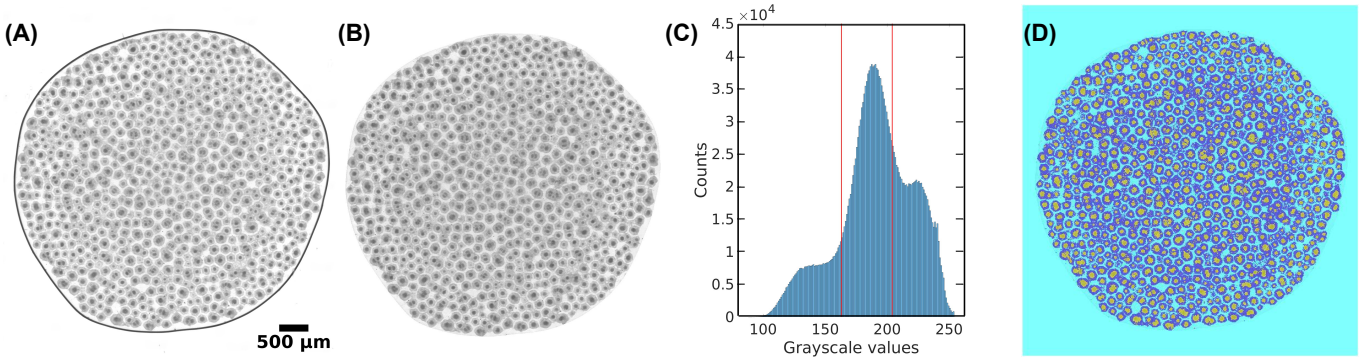

Fig. S3. (A) Representative example for an initial bright-field image of a droplet with protocell patterning. (B) Same droplet after masking (see text for details). (C) Pixel grayscale value histogram inside the droplet, with the two thresholds from Otsu's method indicated by vertical red lines. (D) Multi-thresholded droplet with darkest, intermediate, and brightest pixels assigned with colors yellow, dark blue, and light blue, respectively.

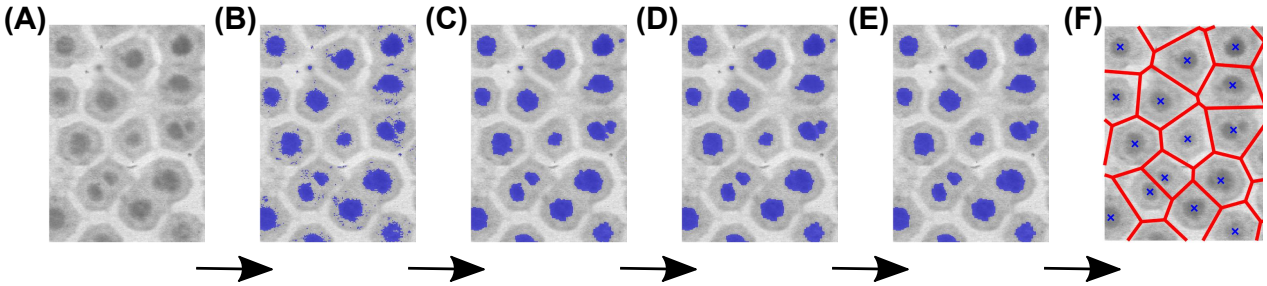

Fig. S4. (A) Close-up of a region with protocells in an extract droplet from bright-field imaging. (B) Same image thresholded according to Fig. S3C,D with the darkest pixels marked in blue. (C) Same after hole-filling and opening with a 3 × 3 square element to remove stray blue pixels. (D) After an additional image closing (same structural element) and intermediate hole-filling, protocell centers appear as single-connected blue area. (E) Filtering according to area histograms (see text) removes outliers. (F) Centroid positions of the obtained centers (blue crosses) support a meaningful Voronoi tesselation (red lines).

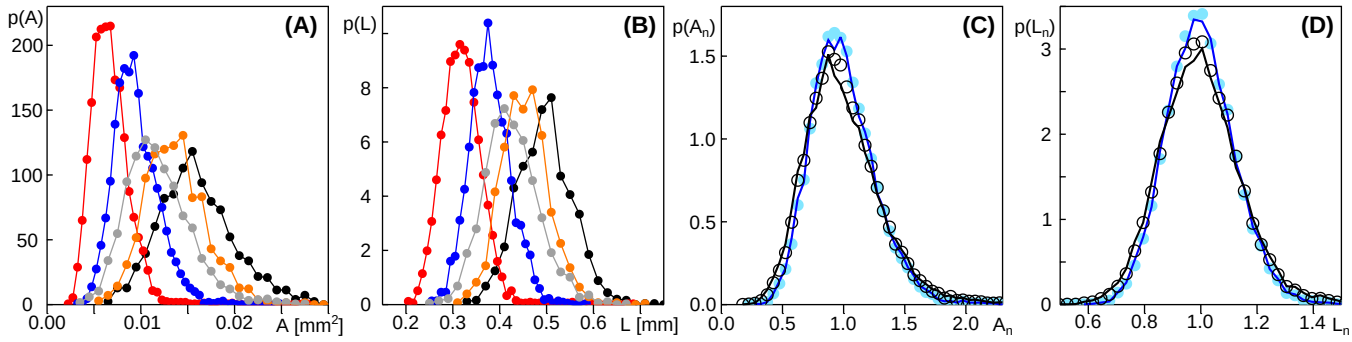

Fig. S5. PDFs of (A) areas and (B) perimeters for different droplets feature similar shapes but different means before normal-ization (data from Fig. 2B,C before normalization; colors indicate different repeats of the assay). The PDFs of (C) normalized areas and (D) perimeters for extracts that have been supplemented with 1 μM taxol or more (black lines and circles) agree well with the data for low and vanishing taxol concentrations ($c \leq 0.1$ μM, blue lines and symbols) right after the onset of pattern formation (lines) and 1-2 h later (symbols). A slight broadening of PDFs for high taxol concentrations most likely is caused by a decreased ratio of protocell size and space between protocells, resulting in an enhanced variability in the image analysis. NB: Data shown in blue are the same as in Fig. 2 of the main text with slightly smaller bin widths for an improved line visibility.

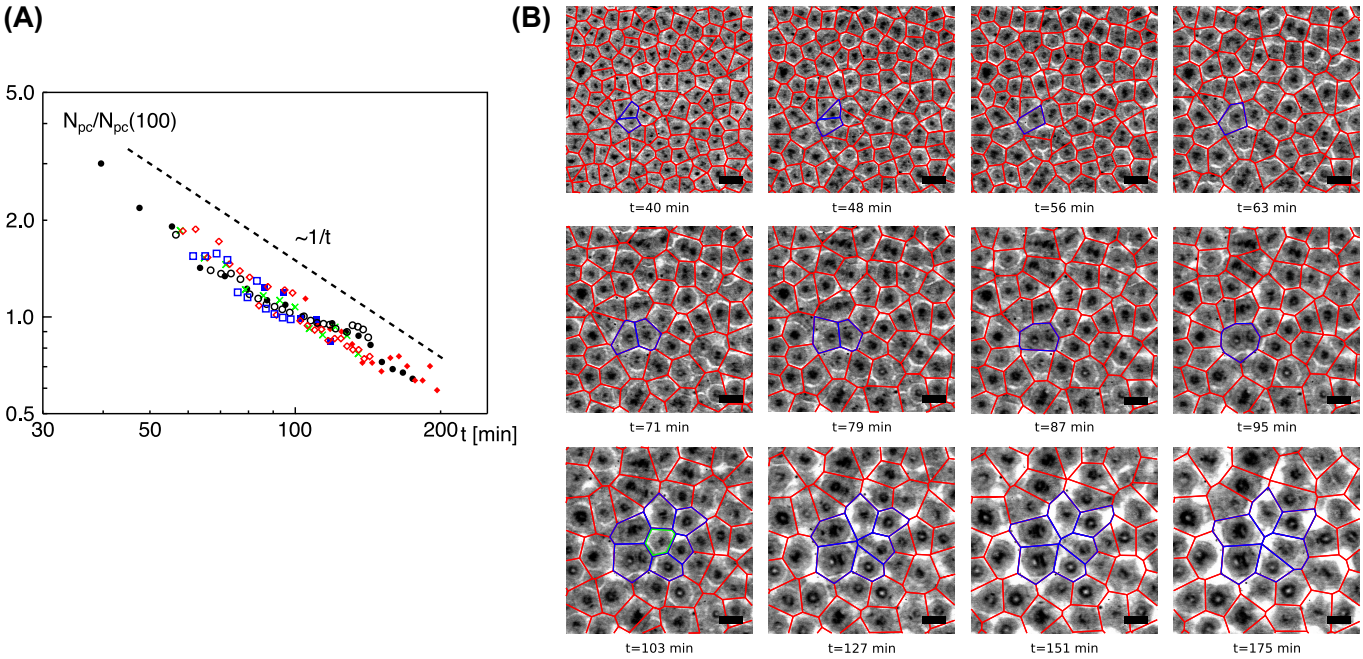

Fig. S6. (A) Complementing Fig. 4A in the main text, the number of protocells, N_{pc} (different droplet preparations/experiments shown as different symbols), normalized by the respective average protocell number at t = 100 min, is seen to follow a power-law decay $\sim 1/t$. This result is an alternative way of representing the linearly increasing average protocell area at a constant total droplet area. (B) Example for the successive coarse-graining of the pattern by merging of protocells; scale bars: 200 μm; see also movie 2.avi for the temporal evolution.

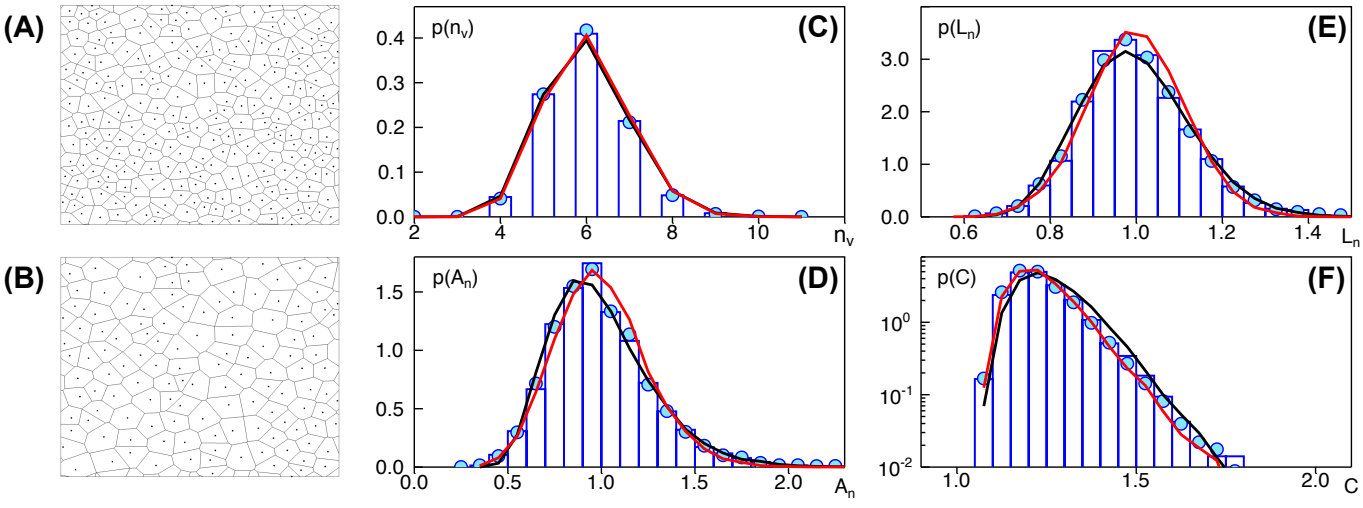

Fig. S7. Applying 500 steps of coarse-graining (i.e. fusion events) to a pattern obtained by model 1 (A), results in a geometrically similar pattern with significantly larger cells (B). This visual impression is confirmed for the PDFs of (C) vertex numbers, $p(n_V)$,(D) normalized cell areas, $p(A_n)$, (E) normalized cell perimeters, $p(L_n)$, and (F) compactness, p(C). Like in Fig. 2 of the main text, blue histograms and symbols represent the experimental data, while the black line reports on the data from model 1 before applying the coarse-graining dynamics. Red lines highlight the result after applying 500 steps of coarse-graining, i.e. 500 fusion events. While minor changes in the shape of the PDFs can be seen after coarse-graining (red vs. black lines), a very good overlap with the experimental data is retained. Data for $\Sigma 2$ also did not show major differences. Therefore, the dominant features of the pattern are preserved after coarse-graining.

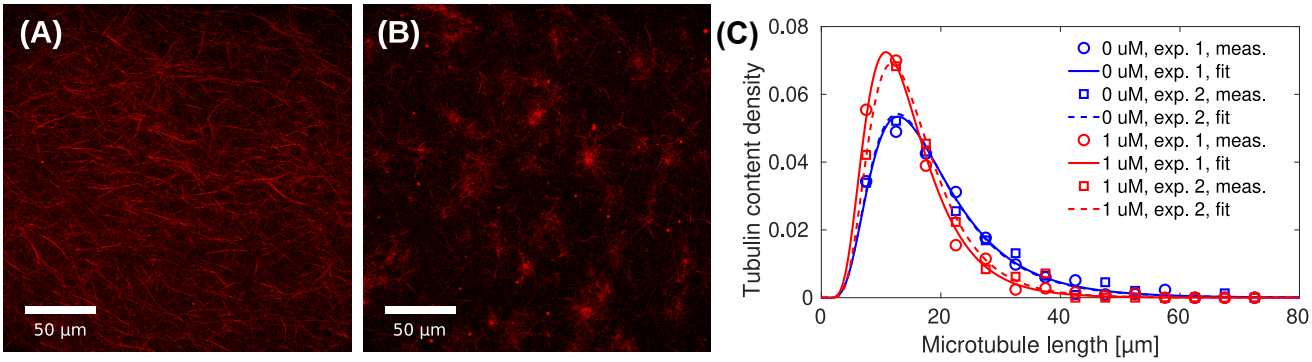

Fig. S8. Fluorescence images of microtubules in early stages of extract self-organization (A) without taxol and (B) with 1 µM taxol (maximum projections of five optical slices, inter-slice distance 500 nm; 8 min and 5 min after sealing the chamber, respectively). While microtubules appear long and quite homogeneously distributed in the absence of taxol, the taxol-treated case features shorter microtubules that assemble already early in protocell-priming focal points (cf. also Fig. S1). (C) Plots of the apparent amount of tubulin (i.e. number of microtubules of a given length times their length) as a function of filament length show a shift of the peak to lower filament lengths in the presence of taxol (red vs. blue symbols and lines). Only small variations are seen when comparing two replicates of either untreated extract (blue symbols) or extracts with 1 µM taxol (red symbols). Full and dashed lines are lognormal functions with mean and variance determined by the raw data: For untreated extracts, the mean length was 14.6 µm and 14.5 µm with standard deviations of 7.9 µm and 8.1 µm, respectively. In the presence of 1 µM taxol, the numbers changed to 12.0 µm and 13.1 µm with standard deviations of 5.8 µm and 6.1 µm. The reduced fraction of long microtubules in the presence of taxol may also be seen when comparing Fig. S2C,D to Fig. S2A,B.

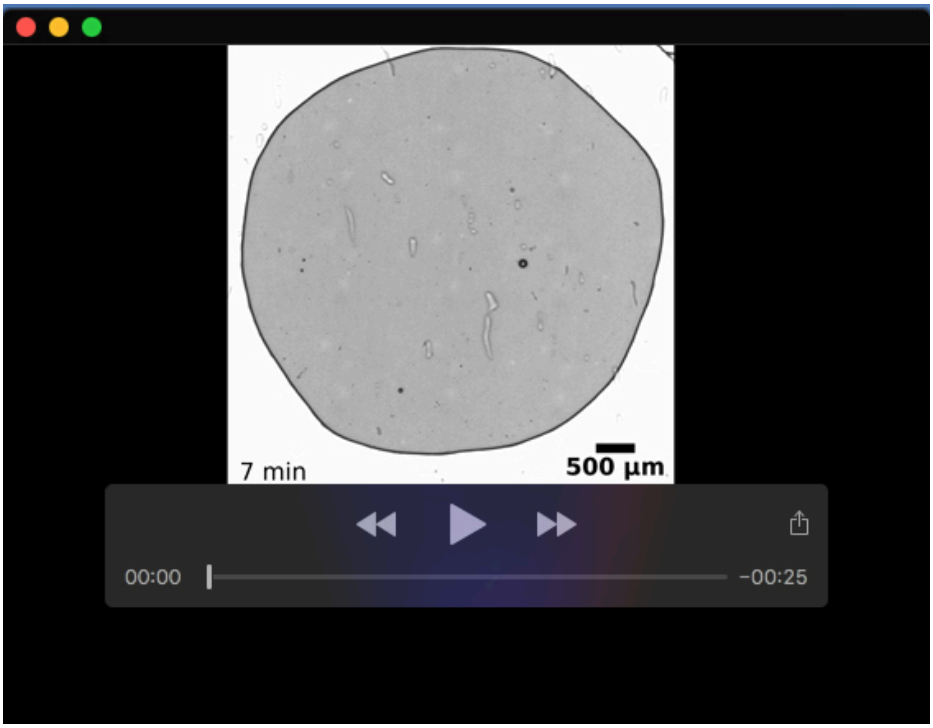

Movie 1. Temporal evolution of the extract droplet shown in Fig. 1 during protocell pattern formation.

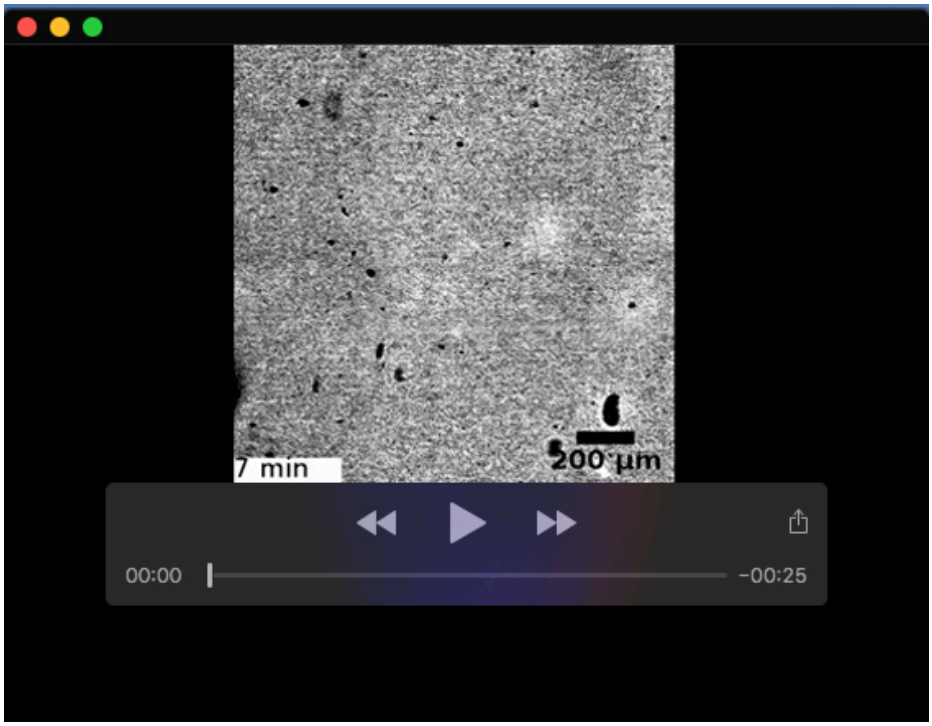

Movie 2. Example for the temporal evolution of pattern coarse-graining shown in Fig. S6B.

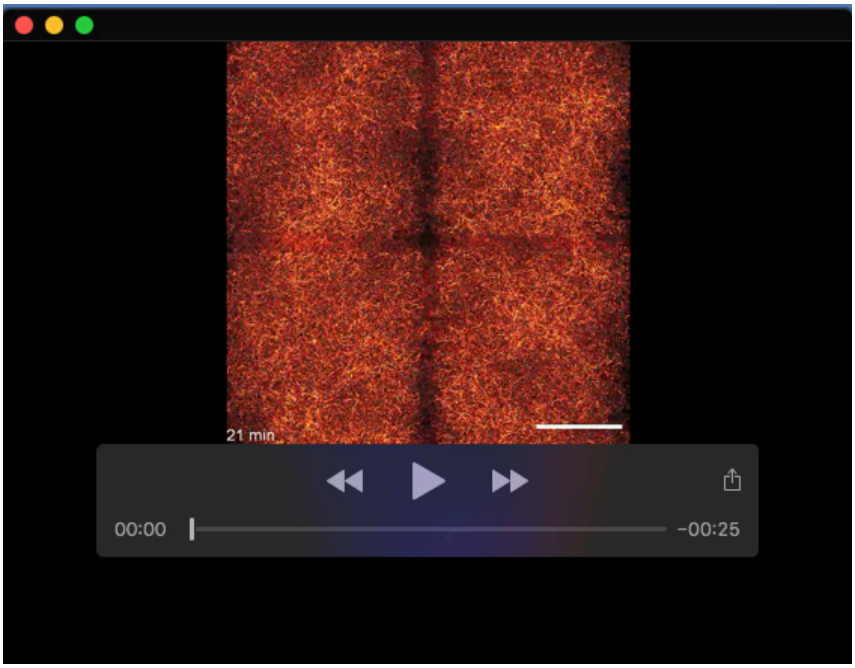

Movie 3. Temporal evolution of fluorescently labeled microtubules in an untreated extract (cf. Fig. S2A,B).

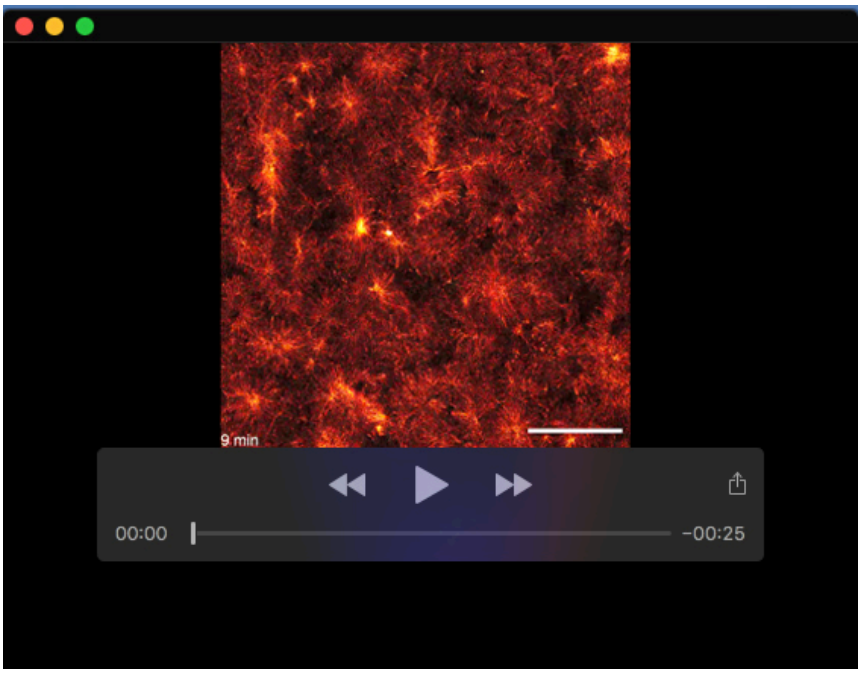

Movie 4. Temporal evolution of fluorescently labeled microtubules in an extract with 1 μM taxol (cf. Fig. S2C,D).